# Surf3DNet1.0: A deep learning model for regional-scale 3D subsurface structure mapping

Zhenjiao Jiang [1,2], Dirk Mallants [2], Lei Gao [2], Gregoire Mariethoz [3], Luk Peeters [4]

1 Key Laboratory of Groundwater Resources and Environment, Ministry of Education, College of Environment and Resources, Jilin University, Changchun, 130021, China

2 CSIRO Land & Water, Locked Bag 2, Glen Osmond, SA 5064, Australia

3 University of Lausanne, Faculty of Geosciences and Environment, Institute of Earth Surface Dynamics, Lausanne, Switzerland

4 CSIRO Mineral Resources, Locked Bag 2, Glen Osmond, SA 5064, Australia

*Corresponding author:* Zhenjiao Jiang (jiangzhenjiao@hotmail.com)

**Abstract.** This study introduces an efficient deep learning approach based on convolutional neural networks with joint autoencoder and adversarial structures for 3D subsurface mapping from surface observations. The method was applied to delineate palaeovalleys in an Australian desert landscape. The neural network was trained on a 6,400 km$^2$ domain by using a land surface tomography as 2D input and an airborne electromagnetic (AEM)-derived probability map of palaeovalley presence as 3D output. The trained neural network has a maximum square error < 0.10 and produces a square error < 0.10 across 93% of the validation areas, demonstrating that it is reliable in reconstructing 3D palaeovalley patterns beyond the training area. Due to its generic structure, the neural network structure designed in this study and the training algorithm have broad application potential to construct 3D geological features (ore bodies, aquifer) from 2D land surface observations.

## 1 Introduction

Imaging the Earth's subsurface is crucial for the exploration and management of mineral, energy and groundwater resources; its reliability depends on the availability and quality of geological data. Although the amount and quality of geological data obtained from borehole logs, geophysical prospecting and remote sensing has increased dramatically over the past decades, their spatial distribution is highly uneven. Most data exist as land surface observations in a limited number of highly-developed areas such as mining and oil fields. Predictive models are much-needed for extracting hidden information from local-scale rich/big datasets for predicting 3D regional-scale subsurface structures in data-poor areas.

Commonly used methods for modelling complex geological structures include geostatistical approaches such as sequential Gaussian or indicator simulation (Lee et al., 2007), transition probability simulation (Felletti et al., 2006; Weissmann and Fogg, 1999), or multiple-point simulation (MPS) methods (Hu and Chugunova, 2008; Mariethoz and Caers, 2014; Strebelle, 2002). However, they often present drawbacks such as not being able to represent elongated and connected geological structures such as palaeovalleys, being inefficient in capturing essential features and patterns from very large training

datasets, or presenting a high computational cost. A fast and reliable tool for high-resolution 3D subsurface imaging based on multiple-support big dataset is still lacking.

Deep learning approaches specialised in big data mining have the potential to fill this gap (Gu et al., 2017; Hinton and Salakhutdinov, 2006; Marcais and de Dreuzy, 2017). Applications in the geosciences include earthquake detection based on seismic monitoring (Mousavi and Beroza, 2019; Perol et al., 2018), or disaster recognition from remote sensing data (Amit et al., 2016; Längkvist et al., 2016), among others. A recent breakthrough in deep learning is the 2D to 3D image processing (Niu et al., 2018; Sinha et al., 2017; Wu et al., 2016; Yi et al., 2017). Such approaches point out a novel way to rapidly and automatically identify covered 3D subsurface structures directly from readily-available 2D surface observations (digital elevation models, land cover maps, signals captured by airborne geophysical surveys).

To this end, we designed a deep convolutional neural network (CNN) with joint autoencoder (Kingma and Welling, 2013) and adversarial structures (Goodfellow et al., 2014). The autoencoder component features large input and output images connected by a small latent space. This structure is advantageous for the fusion of complex input data and 3D image reconstruction. Its training involves direct back-propagation according to a voxel-wise independent heuristic criterion, and thus often needs a large training dataset to constrain the model and avoid overfitting (Laloy et al., 2018). The generative adversarial learning tries to generate multiple images inheriting the probability structure of one real image, which relaxes the need for very large training dataset. The proposed approach successfully generates regional-scale 3D palaeovalley patterns from 2D digital terrain information in an Australian desert landscape, demonstrating that the interplay between autoencoder and adversarial components provides a generic tool to exploit more effectively geophysical, land surface and other data to generate realistic regional-scale 3D geological structures.

## 2 Method

The adversarial neural network for 3D subsurface imaging involves three steps: (1) patch extraction and representation, (2) nonlinear mapping and reconstruction, and (3) statistical expression of the generated image (Fig. 1). The first step is referred to as 'encoder' (Fig. 1a), which is employed to fuse the information contained in the 2D land surface observation images (input data) into a low-dimension layer by successive convolutions (Hinton and Salakhutdinov, 2006):

$$h(\mathbf{x}) = f(\mathbf{W} \cdot \mathbf{x} + \boldsymbol{b}), \tag{1}$$

where $f$ is a nonlinear function referred to as "activation function", $\mathbf{W}$ is a matrix of weights and $\boldsymbol{b}$ is a bias vector in the encoder.

The encoder can be designed to contain multiple layers, where the number of layers is defined as 'depth'. Each layer can contain multiple images, with the number of images defined as 'width'. The images in one layer are convoluted to generate

the elements in the image of the next layer by weight filters, and the elements in the low-dimension layer of the encoder (the output) are called 'code'. The process of convolution is illustrated in Fig. 1b, which shows that with a filter size of 2×2 (for a 2D image convolution for example), one element in the output layer is related to 4 elements in the input layer. Thus, the

60  spatial correlation scale addressed by the convolutional neural network can be controlled by the filter size in both vertical and horizontal directions.

The weight and bias in the encoder are trained to ensure that the code follows a standard normal distribution, by minimizing the Kullback–Leibler divergence ($L1$), defined as (Kullback and Leibler, 1951):

$$L1 = \frac{1}{2N} \sum_{i=1}^{N} (\mu^2 + \sigma^2 - \log \sigma^2 - 1)_i, \tag{2}$$

where $N$ is number of codes in the final output layer of the encoder, $\mu$ and $\sigma$ are the mean and standard deviation of the codes,

65  respectively.
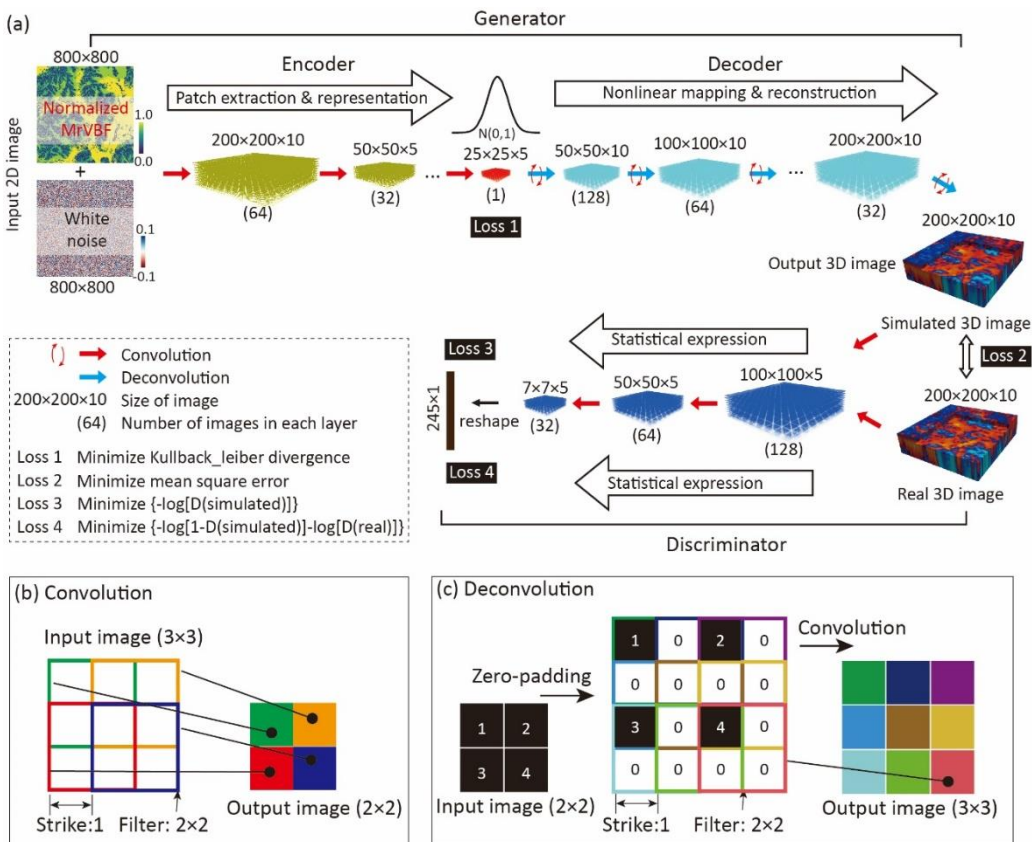
**Figure 1. (a) Adversarial convolution neural network composed of (1) encoder for input images patch extraction and representation, (2) decoder for nonlinear mapping and 3D image reconstruction, (3) discriminator for distinguishing the generated**

70  **3D image and real image after statistical expression; and features of the (b) convolution and (c) deconvolution processes with the colour representing the origin of the deconvoluted values. For mapping palaeovalley patterns in an Australian desert landscape,**

75 **the input data uses the 2D MrVBF (an index calculated from globally available digital elevation model); the output is a 3D probability map of palaeovalley presence. For convenience of 3D convolution, the 2D input image (800×800×1) is simply repeated in 10 layers to form a 3D input dataset (800×800×10). Following a structure optimization by trial-and-error, the encoder is designed to contain 4 layers, with a width of 64, 32, 32 and 1 in each layer, respectively; the decoder contains 6 layers, with a width of 1, 16, 32, 32, 64, and 128, respectively; the discriminator contains 4 layers with a width of 128, 64, 32, 1, respectively.**

In the second step, the codes are converted into a 3D output image by deconvolution (referred to as 'decoder', Fig. 1a), which is a process involving a zero-padding before the convolution (Fig. 1c). The combination of decoder and encoder forms a 'generator', linking input and output images. The generated 3D image is referred to as 'simulated image'.

80 To ensure that the simulated image is comparable to a real image, a voxel-wise independent heuristic criterion is minimized. The mean square error ($L2$) between simulated and real images at all voxels is used as criterion to update the weight and bias in the decoder, which is expressed as:

$$L2 = \frac{1}{M}\|G(\mathbf{z}) - \mathbf{Y}\|^2, \tag{3}$$

where $M$ is the number of voxels in the output 3D image, $\mathbf{Y}$ is the real image, $\mathbf{z}$ is the code generated from the encoder, and $G(\cdot)$ represents the convolutional calculations in the decoder (in the same form as Eq. 1).

85 However, if only a limited number of real 3D images are available to train the network, the use of a voxel-wise independent criterion often leads to an overfitting problem. Goodfellow (2014) proposed a generative adversarial network structure, which adds a 'discriminator' to convert simulated and real images to a vector, respectively, by an identical convolution process (Fig. 1a). Adversarial criteria are proposed, typically expressed by binary cross entropy functions as:

$$L3 = -\frac{1}{V}\log[D(G(\mathbf{z}))], \tag{4}$$

and

$$L4 = -\frac{1}{V}\log[D(\mathbf{Y})] - \frac{1}{V}\log[1 - D(G(\mathbf{z}))], \tag{5}$$

90 where $V$ is the size of the output vector via the discriminator, and $D(\cdot)$ represents the calculations (Eq. 1) in the discriminator. The weights in the discriminator are trained to minimize $L4$, which attempts to distinguish the vectors generated from the real and simulated 3D images. The weights in the generator are trained to minimize $L3$, which attempts to fool the discriminator to be unable to identify the vector generated from the simulated 3D image. In such a way, the generator can produce images aligned with the real image in terms of probability structure (Goodfellow et al., 2014).

95 Finally, while the loss function $L4$ is minimized to optimize the weights in the discriminator, a comprehensive loss function combining $L1$, $L2$ and $L3$ is employed to optimize the weights in the generator, which is expressed as (Wu et al., 2016):

$$L_g = a \cdot L1 + b \cdot L2 + c \cdot L3, \tag{6}$$

where a, b, c are the coefficients on each loss function. This loss function makes it convenient to vary the neural network structure between semi-supervised learning with additional adversarial neural network by defining coefficient c as non-zero value, and supervised learning with merely autoencoder neural network with c as zero.

100 The hyperparameters (including the width, depth, filter size and the coefficients in generator loss functions, etc.) defining the neural network structure, are determined by trial-and-error tests (Supplementary materials). Weight and bias in generator and discriminator are trained to minimize $L_g$ and $L4$ using the stochastic gradient descent algorithm, referred to as adaptive moment estimation (ADAM) (Kingma and Ba, 2014). We implemented the above convolution neural network using the Tensorflow Python library (Abadi et al., 2016). Once the neural network is trained, the 'generator' in the network (Fig. 1a) is

105 used independently to generate 3D subsurface structures from the 2D land surface observations.

## 3 Results

We use a CSIRO dataset to test the effectiveness of our deep-learning approach in predicting 3D palaeovalley patterns in the Anangu Pitjantjatjara Yankunytjatjara (APY) lands of South Australia (Fig. 2a and 2b). The dataset includes a 100-m, 2D Multiple-resolution Valley Bottom Flatness (MrVBF) index (calculated from the digital elevation model) across the entire

110 model domain (Gallant and Dowling, 2003), and a 3D electrical conductivity dataset (400-m horizontal and 10-m vertical resolution) interpreted from an airborne electromagnetic (AEM) survey in the APY Lands (Ley-Cooper and Munday, 2013; Soerensen et al., 2016). Previous hydrogeological characterization indicate that high bulk electrical conductivity values (EC) are a proxy for palaeovalley presence (Jiang et al., 2019; Munday et al., 2013; Taylor et al., 2015). Thus, a palaeovalley aquifer index (PAI) is defined as:

$$PAI = \frac{\log_{10}(EC) - \log_{10}(EC)_{min}}{\log_{10}(EC)_{max} - \log_{10}(EC)_{min}}, \tag{7}$$

115 where *max* and *min* represent the maximum and minimum logarithm of EC values over the entire dataset, respectively. PAI ranges from 0.0 to 1.0 and is calculated in the first 100 m depth at the AEM-surveyed area, which is considered as a ground-truth 3D probability map of palaeovalley occurrences with a spatial resolution of 400 m×400 m×10 m.
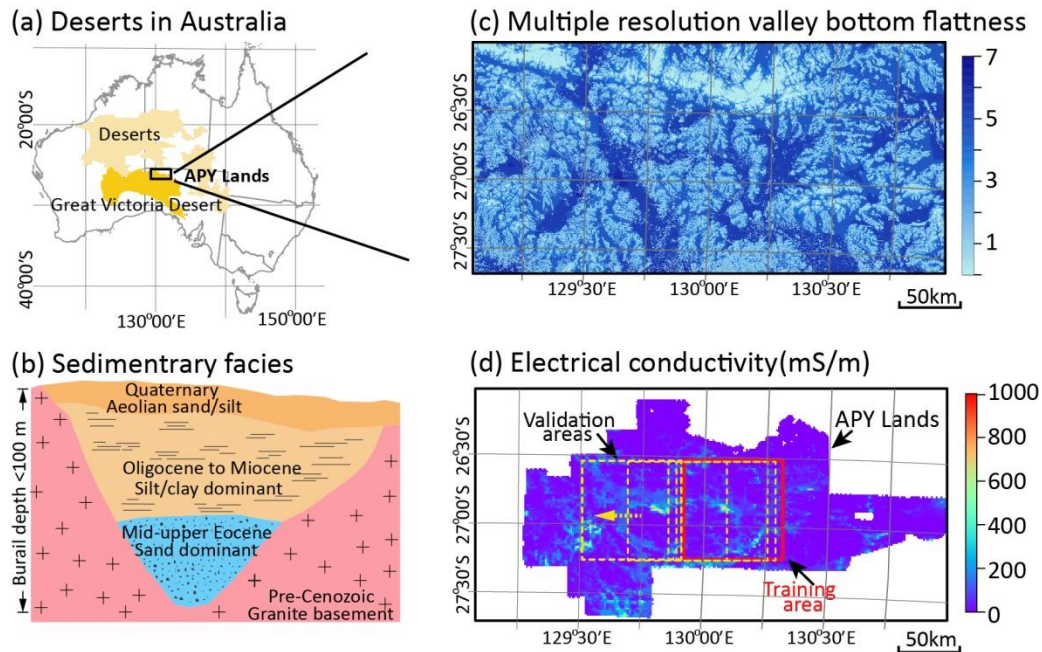
**Figure 2. Datasets for delineating 3D palaeovalley in the Anangu Pitjantjatjara Yankunytjatjara (APY) Lands of South Australia: (a) location of the largest deserts in Australia and (b) general conceptual model of palaeovalley sedimentary facies revealed by over 90% borehole logs, (c) multiple resolution valley bottom flatness index, and (d) electrical conductivity (at depths of 30 to 40 m with a horizontal resolution of 400 m) inferred by airborne electromagnetic surveys in the APY Lands, forming an indicator of palaeovalley occurrence.**

A neural network simulator is established and trained to relate the AEM-derived PAI (output image) with 2D MrVBF data (input image). The training dataset covers part of the APY Lands (6,400 km$^2$) (hereafter referred to as 'training area'). Both loss functions for discriminator and generator were monitored when training the model to verify the network being trained sufficiently (Supplementary materials). Training of the network under 10,000 iterations on a high-performance computer (Tesla P-100-SXM2-M-16GB) required 100 to 150 minutes of computation time. Once trained, generating of 3D image from 2D MrVBF required less than five seconds on a desktop computer.

An area 80 km west of the training area is first used to validate the trained neural network in generating 3D PAI. The statistics of square errors between the simulated 3D PAI and real PAI are calculated at all 200×200×10 voxels. As shown in Fig. 3, the squared error in the training dataset is below 0.1 and with a mean value of about 0.03, and the squared error of the predicted 3D PAI is well below <0.1 for 93% of the validation domain, with a mean squared error of about 0.04. The patterns of the generated palaeovalley in both horizontal and vertical directions align with those inferred from the AEM-derived PAI. This indicates that the deep-learning neural network structure developed in this work is capable of incorporating the relationships between the MrVBF and the buried palaeovalley patterns, and allowing for reliable predictions beyond the training area.
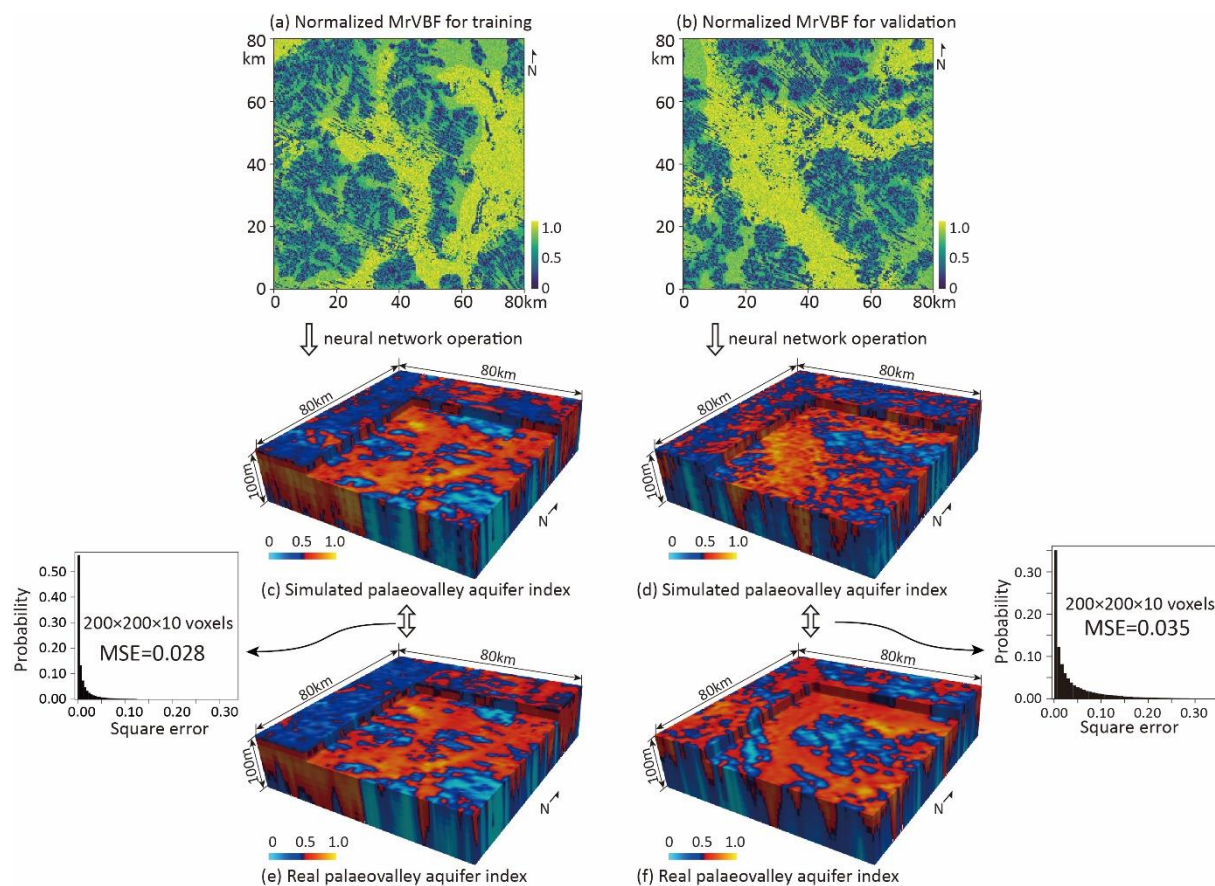
140

**Figure 3. Multiple resolution valley bottom flatness (MrVBF) (a and b) converted to the 3D palaeovalley aquifer index (PAI) in the training area (c) and validation area (80 km west to the train area) (d) by the neural network simulator, compared with AEM-derived PAI (ground truth data) (e) and (f) generated from airborne electromagnetic surveys. The trained neural network with a maximum square error < 0.10 results in a PAI error < 0.10 across 93% of this validation zone, with <1% of this validation zone**
145 **having errors exceeding 0.20.**

Furthermore, another 19 validation areas west to the training domain (Fig. 2d) are used to monitor the decay in the accuracy of predicted palaeovalley patterns. This is done using two different models: semi-supervised learning with additional adversarial neural network and supervised learning with only autoencoder neural network (controlled by coefficient c in Eq. 6).

150 As shown in Fig. 4, an extremely small error (<0.01) can be achieved when constructing palaeovalleys in the training area by supervised learning using only the autoencoder neural network. The mean error resulting from the semi-supervised learning with additional adversarial network is higher, i.e. about 0.03. Within the 19 validation areas, the mean square errors in predicting palaeovalley patterns by both neural networks are well below 0.04.
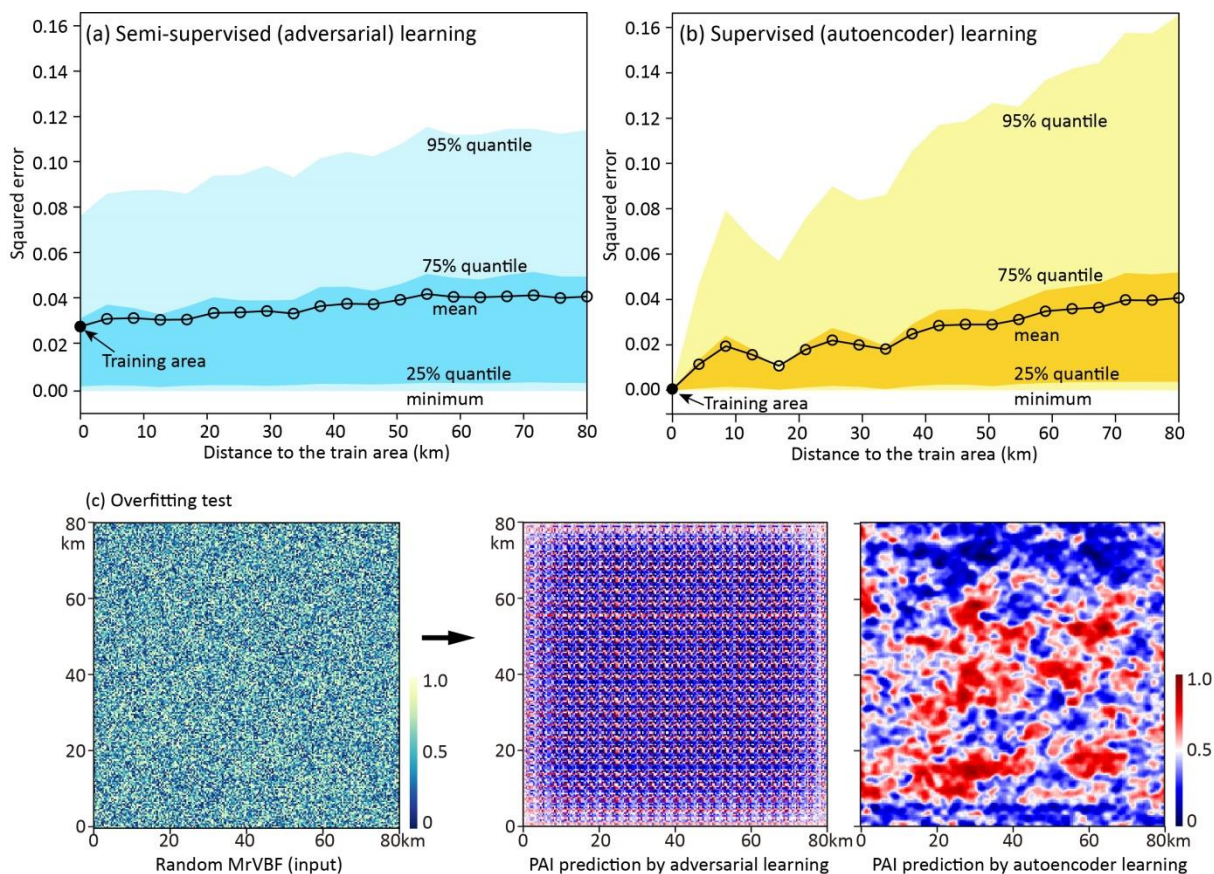
**Figure 4.** Squared errors between the true 3D palaeovalley aquifer index (PAI) directly calculated from AEM-derived electrical conductivity, and PAI predicted by (a) autoencoder neural network using supervised learning and (b) adversarial neural network using semi-supervised learning in the areas west to the training area, with separation distance varying from 0 to 80 km; and (c) an overfitting test with a random 2D MrVBF as input to predict PAI at depth of 30-40 m following adversarial learning and only autoencoder.

While the autoencoder learning generally performs better than the adversarial learning in terms of mean squared errors, its prediction errors (especially the 95% quantile) increase much faster with the separation distance between validation and training areas. This indicates that using the autoencoder only can potentially lead to very large errors (or poor predictions) in case of discrepancies between training and prediction areas. We hypothesize that these errors are due to model overfitting in the case of using only the autoencoder learning. To confirm this, we conduct an overfitting test based on a synthetic ground being a random MrVBF input following a uniform distribution (i.e. non-informative) ranging from 0 to 1, which should result in a uniform PAI distribution. As shown in Fig. 4c, a uniform PAI can be generated by adversarial learning, while the predicted PAI by using only the autoencoder learning results in structured patterns. This means that the weights trained by purely supervised learning inherit too much information hidden in the training dataset, which is inflexible in predicting 3D palaeovalley patterns with strong variations from the input image. On the other hand, adversarial learning is much more

170    robust to discrepancies and the accuracy decays only slightly in predicting 3D structures in areas further away from the training area, which is a highly desired property in real world applications.

## 4 Conclusions

This study developed an efficient and reliable adversarial convolutional neural network simulator for generating 3D subsurface structures directly from 2D land-surface data. The proposed generic structure of the convolutional neural network

175    was composed of an 'encoder' to fuse 2D input data into low-dimension codes following a normal distribution, a 'decoder' to nonlinearly map the low-dimension codes into 3D subsurface images, and a 'discriminator' to statistically express the generated and real subsurface image into a vector for adversarial semi-supervised learning based on a single training image.

The neural network was successfully tested in mapping the 3D palaeovalley systems in the northeast Great Victoria Desert, Australia. Training and validation involved using the multiple resolution valley bottom flatness (MrVBF) (input) and 3D

180    palaeovalley aquifer index (PAI) (output) on an area of $80 \times 80$ km$^2$. The neural network trained to a maximum error <0.1 can predict 3D PAI with errors <0.1 at over 90% of the validation zones.

The outstanding performance of the deep-learning neural network for 3D subsurface structure imaging has applications as a generic novel tool for making better use of existing multiple-support geophysical, land surface, and remote sensing data for better management of limited resources such as groundwater.

185    **Codes/Data Availability**

The original data of MrVBF and AEM were provided by John Gallant and Tim Munday, respectively, and are available freely from CSIRO Data Access Portal https://doi.org/10.4225/08/5701C885AB4FE and https://doi.org/10.25919/5d0868d48591e. The codes for neural network developed in Tensorflow are now provided in https://doi.org/10.7910/DVN/DDEIUV.

190    **Acknowledgement**

Funding support for this study was provided by the National Key R&D Program of China (2018YFB1501803), and the International Postdoctoral Exchange Fellowship Program (2017) from China Postdoctoral Council in combination with CSIRO funding through the Land and Water Business Unit and the Future Science Platform Deep Earth Imaging. We thank Guillaume Rongier and Hoel Seille for the internal review and constructive suggestions on this article.

## References

Abadi, M., Barham, P., Chen, J., Chen, Z., Davis, A., Dean, J., Devin, M., Ghemawat, S., Irving, G., and Isard, M.: Tensorflow: a system for large-scale machine learning, 2016, 265-283.

Amit, S. N. K. B., Shiraishi, S., Inoshita, T., and Aoki, Y.: Analysis of satellite images for disaster detection, 2016, 5189-5192.

Felletti, F., Bersezio, R., and Giudici, M.: Geostatistical simulation and numerical upscaling, to model ground-water flow in a sandy-gravel, braided river, aquifer analogue, Journal of Sedimentary Research, 76, 1215-1229, 2006.

Gallant, J. C. and Dowling, T. I.: A multiresolution index of valley bottom flatness for mapping depositional areas, Water resources research, 39, 2003.

Goodfellow, I., Pouget-Abadie, J., Mirza, M., Xu, B., Warde-Farley, D., Ozair, S., Courville, A., and Bengio, Y.: Generative adversarial nets, 2014, 2672-2680.

Gu, J., Wang, Z., Kuen, J., Ma, L., Shahroudy, A., Shuai, B., Liu, T., Wang, X., Wang, G., and Cai, J.: Recent advances in convolutional neural networks, Pattern Recognition, 2017. 2017.

Hinton, G. E. and Salakhutdinov, R. R. J. s.: Reducing the dimensionality of data with neural networks, 313, 504-507, 2006.

Hu, L. and Chugunova, T.: Multiple-point geostatistics for modeling subsurface heterogeneity: A comprehensive review, Water Resources Research, 44, 2008.

Jiang, Z., Mallants, D., Peeters, L., Gao, L., Soerensen, C., and Mariethoz, G.: High-resolution paleovalley classification from airborne electromagnetic imaging and deep neural network training using digital elevation model data, Hydrology and Earth System Sciences, 23, 2561-2580, 2019.

Kingma, D. P. and Ba, J.: Adam: A method for stochastic optimization, arXiv preprint arXiv:1412.6980, 2014.

Kingma, D. P. and Welling, M.: Auto-encoding variational bayes, International Conference on Learning Representations, 2013.

Kullback, S. and Leibler, R. A.: On information and sufficiency, The annals of mathematical statistics, 22, 79-86, 1951.

Laloy, E., Hérault, R., Jacques, D., and Linde, N.: Training-Image Based Geostatistical Inversion Using a Spatial Generative Adversarial Neural Network, Water Resources Research, 54, 381-406, 2018.

Längkvist, M., Kiselev, A., Alirezaie, M., and Loutfi, A.: Classification and segmentation of satellite orthoimagery using convolutional neural networks, Remote Sensing, 8, 329, 2016.

Lee, S.-Y., Carle, S. F., and Fogg, G. E.: Geologic heterogeneity and a comparison of two geostatistical models: Sequential Gaussian and transition probability-based geostatistical simulation, Advances in water resources, 30, 1914-1932, 2007.

Ley-Cooper, A. and Munday, T.: Groundwater Assessment and Aquifer Characterization in the Musgrave Province, South Australia: Interpretation of SPECTREM Airborne Electromagnetic Data, Goyder Institute for Water Research Technical Report Series, 2013. 2013.

Marcais, J. and de Dreuzy, J. R.: Prospective Interest of Deep Learning for Hydrological Inference, Groundwater, 55, 688-692, 2017.

Mariethoz, G. and Caers, J.: Multiple-point geostatistics: stochastic modeling with training images, John Wiley & Sons,
230   2014.

Mousavi, S. M. and Beroza, G. C.: A Machine-Learning Approach for Earthquake Magnitude Estimation, Geophysical Research Letters, 2019. 2019.

Munday, T., Abdat, T., Ley-Cooper, Y., and Gilfedder, M.: Facilitating Long-term Outback Water Solutions (G-FLOWS Stage-1: Hydrogeological Framework, Goyder Institute for Water Research Technical Report Series, 2013. 2013.

235   Niu, C., Li, J., and Xu, K.: Im2Struct: Recovering 3D Shape Structure from a Single RGB Image, structure, 4096, 80, 2018.

Perol, T., Gharbi, M., and Denolle, M.: Convolutional neural network for earthquake detection and location, Science Advances, 4, e1700578, 2018.

Sinha, A., Unmesh, A., Huang, Q., and Ramani, K.: SurfNet: Generating 3D shape surfaces using deep residual networks, 2017.

240   Soerensen, C. C., Munday, T. J., Ibrahimi, T., Cahill, K., and Gilfedder, M.: Musgrave Province, South Australia: processing and inversion of airborne electromagnetic (AEM) data: Preliminary results. 1839-2725, Goyder Institute for Water Research Technical Report Series, 2016.

Strebelle, S.: Conditional simulation of complex geological structures using multiple-point statistics, Mathematical Geology, 34, 1-21, 2002.

245   Taylor, A., Pichler, M., Olifent, V., Thompson, J., Bestland, E., Davies, P., Lamontagne, S., Suckow, A., Robinson, N., and Love, A.: Groundwater Flow Systems of North-eastern Eyre Peninsula (G-FLOWS Stage-2): Hydrogeology, geophysics and environmental tracers, Goyder Institute for Water Research Technical Report Series, 2015. 2015.

Weissmann, G. S. and Fogg, G. E.: Multi-scale alluvial fan heterogeneity modeled with transition probability geostatistics in a sequence stratigraphic framework, Journal of Hydrology, 226, 48-65, 1999.

250   Wu, J., Zhang, C., Xue, T., Freeman, B., and Tenenbaum, J.: Learning a probabilistic latent space of object shapes via 3d generative-adversarial modeling, 2016, 82-90.

Yi, L., Shao, L., Savva, M., Huang, H., Zhou, Y., Wang, Q., Graham, B., Engelcke, M., Klokov, R., and Lempitsky, V.: Large-scale 3d shape reconstruction and segmentation from shapenet core55, arXiv preprint arXiv:1710.06104, 2017. 2017.